

Characterization of Sol–Gel LiMn_2O_4 Spinel Phase

V. Massarotti,¹ D. Capsoni, M. Bini, and G. Chiodelli

Dipartimento di Chimica Fisica and CSTE-CNR, Università di Pavia, via Taramelli 16, I-27100 Pavia, Italy

C. B. Azzoni and M. C. Mozzati

INFN, Dipartimento di Fisica “Alessandro Volta,” Università di Pavia, via Bassi 6, I-27100, Pavia, Italy

and

A. Paleari

INFN-Dipartimento di Scienza dei Materiali, Università di Milano, via Cozzi 53, I-20125 Milano, Italy

Received December 31, 1998; in revised form May 19, 1999; accepted May 28, 1999

Lithium manganese spinel $\text{Li}_{1+y}\text{Mn}_{2-y}\text{O}_4$ ($0.0 \leq y \leq 0.07$) synthesized by the sol–gel process is studied with a focus on the effects of the changes of formation conditions which can sensibly determine the mean crystallite size from a few nanometers to several hundred nanometers. Changes of stoichiometry and abundance of the spinel phase can be observed in the $573 \leq T_A$ (K) ≤ 1073 range of annealing temperature (T_A). Comparing spinel phases obtained by sol–gel and solid state synthesis evidences the correlation among composition, structure, and electric and magnetic properties. © 1999 Academic Press

Key Words: LiMn_2O_4 , spinel; $\text{Li}_{1+y}\text{Mn}_{2-y}\text{O}_4$, Li-rich spinel; LiMn_2O_4 , crystallite size and strain; LiMn_2O_4 , electric properties; LiMn_2O_4 , magnetic properties.

1. INTRODUCTION

A great deal of work has been done on compounds of the Li–Mn–O system, because of the peculiar applications of LiMn_2O_4 spinel and related phases in the fields of electrochemistry (1–4) and catalysis (5–7).

Both stoichiometric (lithium cationic fraction $x = 0.333$) and nonstoichiometric spinel phases in samples with $x > 0.333$ and $x < 0.333$ (Li-rich and Li-poor samples, respectively) were recently studied. As a result, new structural-calorimetric (8) and structural-spectroscopic (9, 10) data are now available on composition-related defects involving Li^+ ions. Samples can be obtained from the solid state reactive system $\text{MnO}/\text{Li}_2\text{CO}_3$ (11–13), or from different reactive systems such as $\text{MnO}_2/\text{Li}_2\text{CO}_3$ (14, 15) and MnO_2/LiOH (16, 17) at temperature higher than 1000 K.

¹ To whom correspondence should be addressed.

An alternative method to synthesize lithium manganese spinel at lower temperature is represented by the sol–gel route (1, 18, 19). Starting from aqueous solutions of LiOH and Mn(II) acetate as precursor, Barboux *et al.* (1) prepared LiMn_2O_4 at temperature as low as 573 K. Following such very soft conditions, the synthesis would lead to a very small particle size. A study of physical and chemical properties of such a phase as a function of the annealing conditions would be extremely interesting since electrical conductivity and magnetic susceptibility may be particularly sensitive to small changes of stoichiometry brought about by modifying the synthesis conditions.

The first aim of the present paper was the study of structural and microstructural properties of the lithium manganese spinel phase obtained from sol–gel synthesis compared with the properties observed in samples obtained from a solid state process. Conductivity, electron paramagnetic resonance, and static magnetic susceptibility measurements were also performed since, as observed in previous works (13, 20, 21), large variations of physical properties can be foreseen as a function of composition and then of mean oxidation state of the transition cation. A clear understanding of the relative behavior of this phase would have importance in catalysis and electrochemical applications.

2. EXPERIMENTAL

2.1. Materials and Sample Preparation

A set of samples with lithium cationic fraction $x = \text{Li}/(\text{Li} + \text{Mn}) = 0.333$ has been synthesized via a sol–gel process, following the procedure proposed by Barboux *et al.* (1). The xerogel precursor was pretreated at 523 K; then it

was divided into five fractions which were heated for 8 h at different temperatures, 573, 673, 873, 973, and 1073 K respectively. These sol-gel samples will be referred as SG573, SG673, SG873, SG973, and SG1073.

Samples were also prepared by solid state reaction from the reactive system Alfa (99.9%) MnO/Carlo Erba (R.P.) Li_2CO_3 , with $x = 0.333$ as previously described (11). In the following, the sample obtained at 1073 K will be referred to as SS1073. An Li-rich sample was obtained by adding an appropriate quantity of Li_2CO_3 to SS1073 to reach $x = 0.37$. The mixture was annealed at 723 K: this sample will be named SS1073R.

Samples for conductivity measurements were prepared by pressing powder with an uniaxial Weber PW40 press into the form of bars ($2 \times 3 \times 10$ mm). They were then sintered for 12 h in air at the same temperature, T_A , used for the annealing process and slowly cooled (5 K/min) to room temperature (RT). The four electrical contacts were obtained by using a conductive silver paint.

2.2. Apparatus and Procedures

The instrumentation for X-ray diffractometry (XRD), conductivity, static magnetic susceptibility, and electron paramagnetic resonance (EPR) measurements has been pre-

viously described (12, 21). EPR (in the X band at 9.31 GHz) and static magnetic susceptibility measurements were performed in the temperature ranges 4–500 K and 4–300 K, respectively.

Structural and microstructural analysis of XRD patterns ($\text{CuK}\alpha$ radiation, $K\alpha_1 = 1.54056 \text{ \AA}$ and $K\alpha_2 = 1.5443 \text{ \AA}$) was carried out following the Rietveld method, according to the procedure already reported (11, 21). Refinement of cationic occupancy factors was not performed because of the strong influence of microstructural parameters on the broadening and position of the peaks with decreasing T_A .

3. RESULTS

3.1. XRD

XRD patterns of samples obtained from the sol-gel route display the expected lines of LiMn_2O_4 phase, as shown in Fig. 1. The abundance of spinel-type phase is increased by increasing T_A , while the content of manganese oxides (Mn_2O_3 and Mn_5O_8), present as impurities, decreases. At the same time, the spinel peaks narrow and shift toward lower angles with increasing T_A (inset of Fig. 1). After the annealing at 1073 K, only the peaks pertinent to the spinel phase are present. One, two, or three phases were included in the structural model for the Rietveld profile refinement,

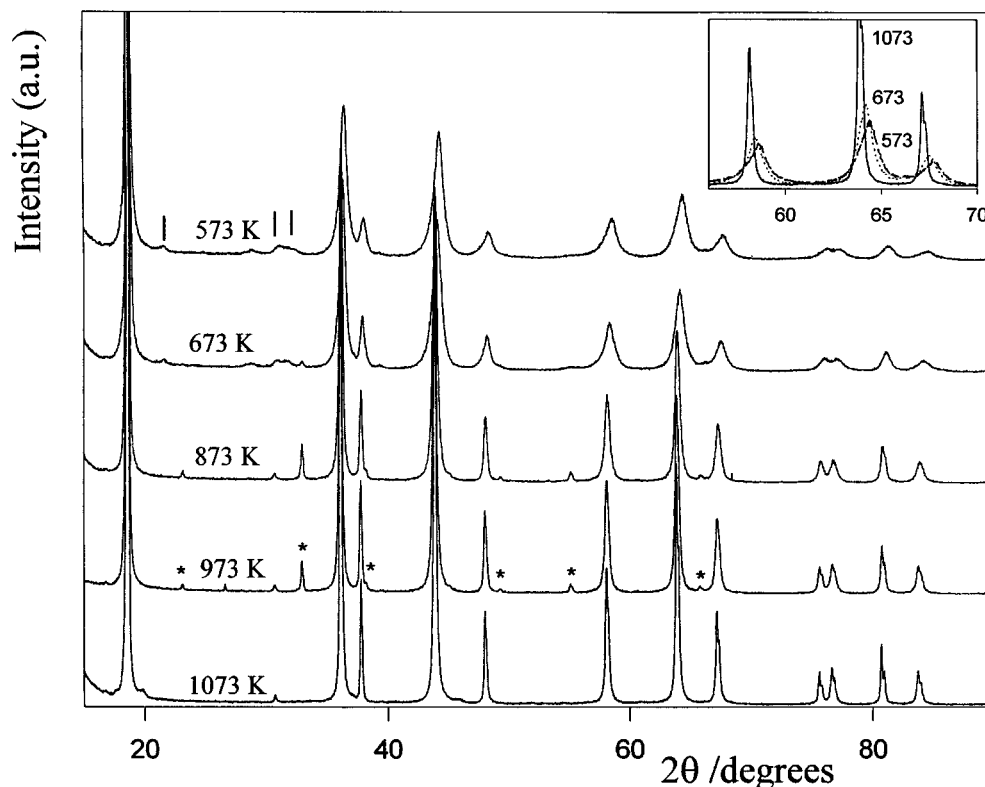


FIG 1. XRD patterns of the samples synthesized via the sol-gel method annealed at different temperatures. Positions of the main peaks of Mn_5O_8 and Mn_2O_3 are marked with bars and stars, respectively. In the inset some profile details are shown.

TABLE 1

Spinel Lattice Parameter, y , Li-enrichment, Phase Percentages, and Discrepancy Factors as Obtained from Rietveld Profile Refinement

Sample	SS1073R	SG573	SG673	SG873	SG973	SG1073
R_p	11.96	7.96	8.45	9.08	8.39	9.92
R_{wp}	16.17	10.46	11.04	11.57	10.60	12.76
S	2.02	2.32	2.42	2.53	2.35	2.76
Spinel						
a (Å)	8.2020(2)	8.191(2)	8.210(1)	8.2354(4)	8.2409(3)	8.2420(3)
y	0.11	0.07(1)	0.03(1)	0.02(1)	0.02(1)	0.00
%	100.00	91.11	96.44	97.80	98.05	100.00
R_B	4.03	2.44	2.40	3.03	3.03	4.10
Mn_2O_3						
%			0.83	2.20	1.95	
R_B			11.32	18.53	23.59	
Mn_5O_8						
%		8.89	2.73			
R_B		11.01	11.65			

depending on the impurities found after each thermal treatment. Phase percentages, discrepancy factors (R_p , R_{wp} , R_B , and goodness of fit S as defined in (22)), and spinel lattice parameters are reported in Table 1. The total amount of impurity phases evaluated with the Rietveld method rapidly decreases with increasing T_A (Fig. 2a).

The spinel cubic lattice parameter a vs T_A is reported in Fig. 2b: a reaches the same value for the SS1073 and for other solid state samples prepared at $T_A > 1073$ K (11). It can be observed that the a values for samples sintered at $T_A < 1073$ K are lower than that reported for the stoichiometric spinel ($a = 8.247$ Å (23, 11)). The same effect is also observed for the a value pertinent to the SS1073 R sample. This fact can be related to the lithium enrichment of the spinel phase (11). The Li excess y in the formula $\text{Li}_{1+y}\text{Mn}_{2-y}\text{O}_4$ was deduced on the basis of the overall cationic fraction x and of the phase abundance for each sample (see Table 1). The SS1073R sample was taken as an Li-rich reference sample ($y = 0.11$) without impurity phases (Table 1).

The rapid decrease of full width at half maximum (FWHM) of the peaks with increasing T_A (see Fig. 1 and inset) indicates the increase in the growing rate of the crystallites during the annealing process. To obtain reliable microstructural parameters we used the LS1 program (24): it is based on the Rietveld method and uses Fourier analysis to take into account the peak broadening due to small crystallite size and microstrain, when the instrumental dependence of FWHM on 2θ is known. LS1 performs refinement of structural and microstructural disorder parameters

using crystallite size and root mean square microstrain as fitting parameters.

For the cubic spinel the constraints for crystallite size components $M_{11} = M_{22} = M_{33}$ and $M_{12} = M_{13} = M_{23}$ and for microstrain components $\varepsilon_{11} = \varepsilon_{22} = \varepsilon_{33}$ and $\varepsilon_{12} = \varepsilon_{13} = \varepsilon_{23}$ were used according to symmetry considerations (25). In Fig. 3 the trend of microstructural parameters obtained from sol-gel samples is compared with that of samples prepared from solid state reaction at $T_A \geq 1073$ K (25). Larger M_{ii} and M_{ij} values are obtained from solid state

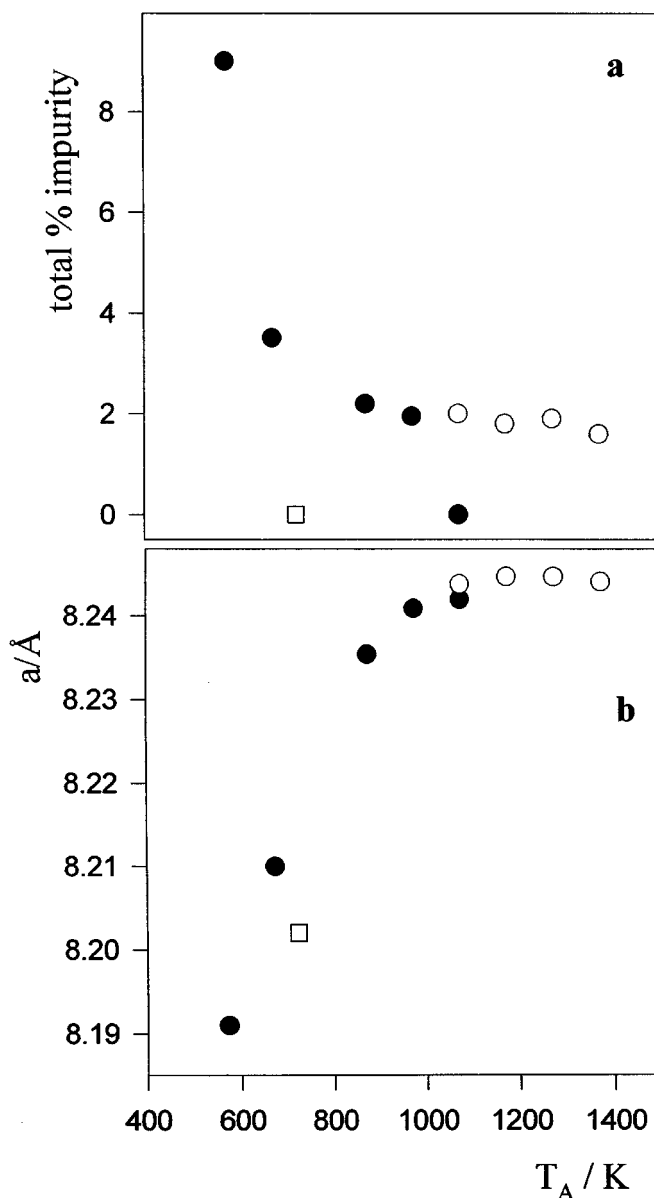


FIG. 2. (a) Total impurity phase percentage and (b) lattice parameter of the spinel phase in samples prepared at different T_A . Full and open circles represent the data for sol-gel and solid state samples, respectively; for the SS1073R sample the square is used.

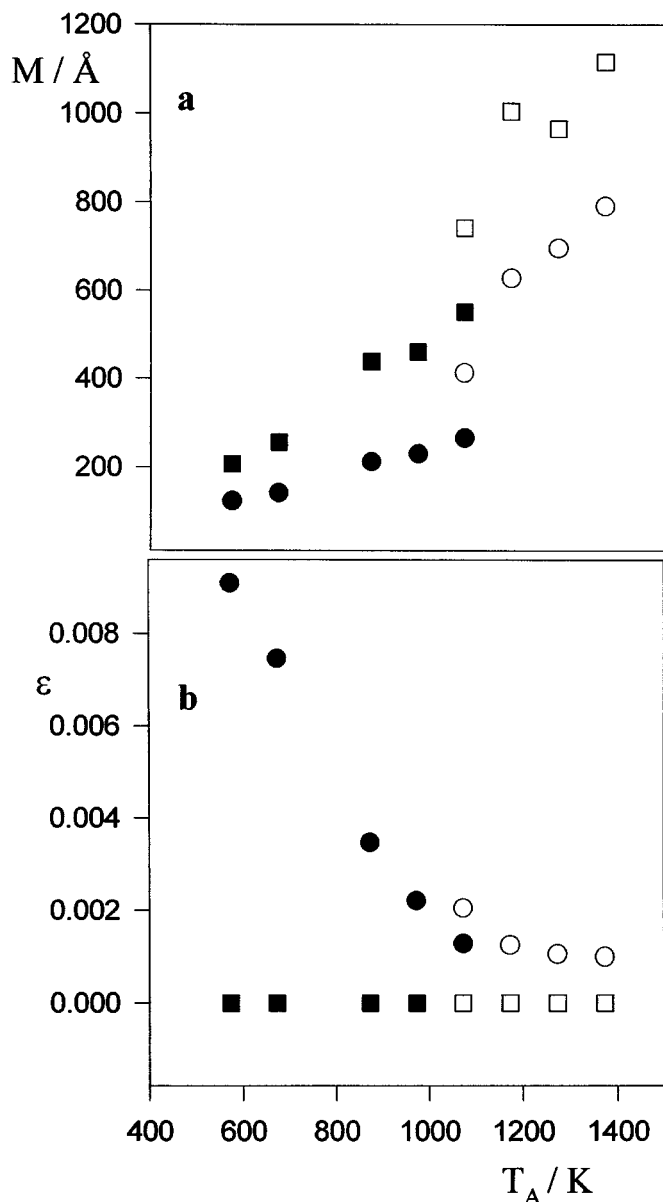


FIG. 3. Trends of (a) M_{ij} (squares) and M_{ii} (circles) and (b) ϵ_{ij} (squares) and ϵ_{ii} (circles) as a function of T_A . Full and open symbols refer to sol-gel and solid state samples, respectively.

synthesis at the same T_A (1073 K), and a faster growing rate of crystallites achieved by increasing T_A can be inferred (Fig. 3a). Figure 3b shows the rapid decrease of ϵ_{ii} values with increasing T_A , reaching at $T_A = 1073$ K approximately the same value observed in samples obtained from solid state reaction. No difference can be observed by comparing ϵ_{ij} values.

Size and strain effects become quite evident in the FWHM values of the different hkl plane families and may be evaluated for different directions of the crystallites according to Lutterotti and Scardi (24). On this basis we can

estimate the mean crystallite size and microstrain vs T_A for different crystallographic families of planes. The slowest increase of crystallite size with the temperature is observed in the $h00$ direction, where the thermal-induced decrease of microstrain is more evident.

3.2. Conductivity

The results of the conductivity measurements are summarized in Fig. 4. The SG1073 sample, showing a transition temperature around 275 K related to the Jahn-Teller distortion of $(\text{Mn}^{3+}\text{O}_6)$ octahedra (21, 26, 27), approaches the behavior of the SS1073 sample (lines *f* and *a*, respectively, in Fig. 4) (21) and, consequently, can be considered stoichiometric. Activation energy of 0.40 eV at $T > 290$ K is deduced for SG1073, as observed in SS1073 (21).

Different behavior is given by sol-gel samples annealed at $T_A < 1073$ K; they show no transition, at least at $T \geq 250$ K, but only a small variation of the slope.

Higher conductivity values observed at $T \geq 290$ K in samples treated at higher T_A (Fig. 4) are consistent with the lower content of insulating spurious phases.

3.3. EPR

At room temperature, the analyzed sol-gel samples show a broad EPR signal with g -factor $g \leq 2$ and with linewidth $\Delta B \cong 0.215$ T for SG573 and $\Delta B \cong 0.330$ T for the samples prepared at higher T_A . The solid state samples show similar

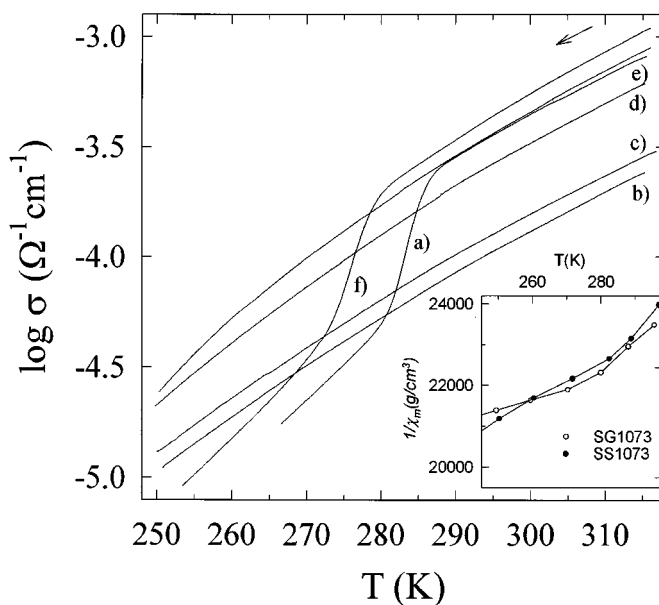


FIG. 4. Conductivity data of (a) SS1073, (b) SG573, (c) SG673, (d) SG873, (e) SG973, and (f) SG1073 samples. In the inset the behavior of $1/\chi_m$ of SS1073 and SG1073 is reported approximately in the same range of temperature.

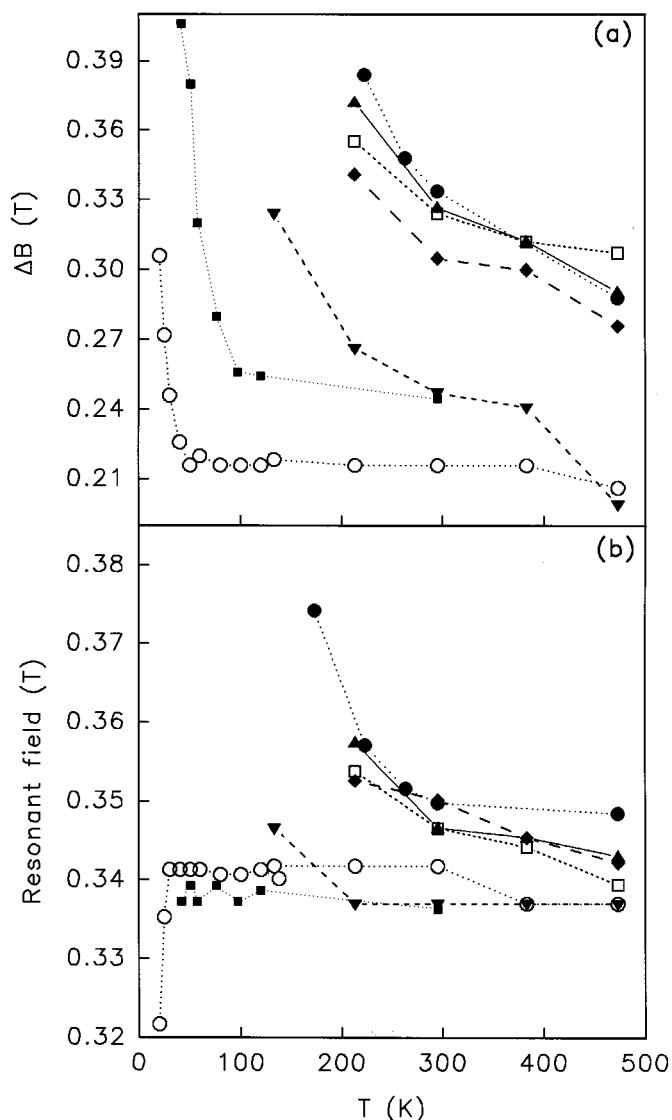


FIG. 5. (a) ΔB and (b) RF as a function of T for the EPR signal of SG573 (\circ), SG673 (\blacktriangledown), SG873 (\square), SG973 (\blacktriangle), SG1073 (\blacklozenge), SS1073 (\bullet), and SS1073R (\blacksquare) samples. The lines are included to guide to the eye. The error in ΔB is about ± 0.012 T for $\Delta B \cong 0.2$ T and about ± 0.025 T for $\Delta B \cong 0.38$ T. The mean error in RF is ± 0.005 T.

EPR signals at $g \leq 2$ with $\Delta B \cong 0.330$ T for SS1073 and $\Delta B \cong 0.250$ T for SS1073R.

Figures 5a and 5b show ΔB and resonant field (RF) values, respectively, at different T . A progressive increase of ΔB with decreasing T is typical of sol-gel samples prepared with $T_A > 800$ K and of the SS1073 sample. An analogous trend may be observed in SG673, but with smaller ΔB values. For SG573, ΔB is nearly independent of temperature, similarly to what was observed in SS1073R, and abruptly increases in the lower temperature range. The EPR lineshape of SG573 and SS1073R is nearly Lorentzian,

while the other samples show an increasing Gaussian character with increasing T_A .

3.4. Static Magnetic Susceptibility

The magnetic behavior of SG1073 is consistent with that of the stoichiometric spinel phase observed in samples produced from solid state reaction like the SS1073, reported and discussed in (20). A slight slope variation is observed in the temperature region of the conductivity anomaly near RT, related to the Jahn-Teller transition (see inset in Fig. 4).

Slightly different features are observed in sol-gel samples prepared at lower T_A . In Fig. 6 mass susceptibility (χ_m) and $1/\chi_m$ data of the SG573 sample in the range 4–300 K are shown and compared with the data of the SS1073R sample. At high temperature the $1/\chi_m$ vs T behavior is nearly linear, with negative intercepts, following the Curie-Weiss law

$$\frac{1}{\chi_m} = \frac{T - \theta}{C_m}, \quad [1]$$

where C_m is the Curie constant and θ is the Weiss constant.

4. DISCUSSION

A strong dependence of a on the annealing temperature has been shown in Fig. 2b. The unusually low a value in samples annealed at temperature as low as 573 and 673 K may be related to the presence of Li-rich spinel phase, according to the variation of the cell parameter as a function

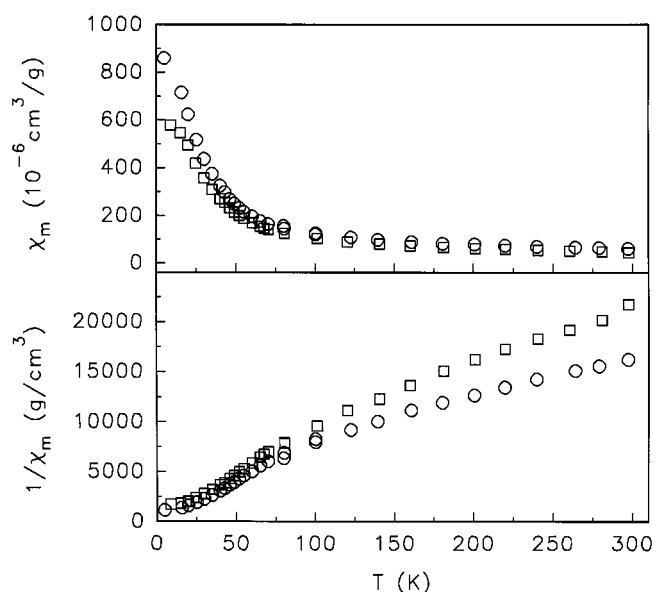


FIG. 6. The χ_m and $1/\chi_m$ curves vs T of the SG573 (circles) and SS1073R (squares) samples.

of the stoichiometry deviation y in $\text{Li}_{1+y}\text{Mn}_{2-y}\text{O}_4$ (12). The presence of lithium excess in the spinel phase also agrees with the observation of nonlithiated manganese oxides in the samples annealed at low temperature (Fig. 2a). The calculated values of y , reported in Table 1, may support a two-step mechanism for the formation of stoichiometric spinel in sol-gel samples:

(I) Formation of Li-rich spinel and manganese oxides (with various manganese oxidation states);

(II) Solid state reaction among these intermediate components to give the stoichiometric LiMn_2O_4 with increasing T_A .

The first evidence which agrees with this model is the lack in samples prepared at $T_A < 1073$ K of the abrupt variation of conductivity near RT attributed to the cooperative Jahn-Teller effect. As already shown, the Jahn-Teller structural transition is only observed in stoichiometric or quasi-stoichiometric samples with small Li-deficiency (8, 26). So, conductivity measurements evidence very small stoichiometry deviations from the stoichiometric composition (compare SG973 ($y = 0.02$) and SG1073 ($y = 0.0$) samples in Fig. 4) that EPR measurements cannot directly reveal.

Nevertheless, EPR measurements are useful to characterize the progressive Li-enrichment in the samples obtained from synthesis at lower temperature. In fact, smaller ΔB values (Fig. 5a) are expected from sol-gel samples with larger Li-enrichment, similar to what was observed for the samples SS1073R and SS1073 prepared by solid state reaction. Besides, exchange narrowing, resulting from coupling of identical ions (28), is suggested by the narrower EPR signal and the nearly Lorentzian lineshape of the SS1073R and SG573 samples. This is consistent with the larger amount of Mn^{4+} ions responsible for the EPR signal of the spinel phase (12), resulting from Li-enrichment.

Further confirmation of the Li-enrichment of the spinel phase of SG573 may be derived by susceptibility measurements. The SG573 sample shows an experimental effective magnetic moment $m_{\text{exp}} = 4.37 \mu_B$. This value, inserted in the relation

$$m_{\text{spinel}}^2 = \frac{m_{\text{exp}}^2 - s m_{\text{Mn}_5\text{O}_8}^2}{1 - s}, \quad [2]$$

where s is the Mn_5O_8 fraction and $m_{\text{Mn}_5\text{O}_8} = 4.80 \mu_B$ (from the compositional model $\text{Mn}_2^{2+}\text{Mn}_3^{4+}\text{O}_8$ (29)), gives rise to $m_{\text{spinel}} = 4.32 \mu_B$. This value (pertaining to the only spinel phase) agrees with the m_{spinel} value calculated by the relation (13)

$$m_{\text{spinel}}^2 = \frac{1}{2 - y} [(1 - 3y)m_{\text{Mn}^{3+}}^2 + (1 + 2y)m_{\text{Mn}^{4+}}^2], \quad [3]$$

for $y = 0.07$, as obtained by XRD (Table 1).

In [3] we assumed $m_{\text{Mn}^{3+}}^2 = 24 \mu_B^2$, based on the hypothesis of high-spin ($S = 2$) Mn^{3+} configuration (21). This is also in agreement with a recent study (7), different from that of Schutte *et al.* (30),² calling for the coexistence of high- and low-spin Mn^{3+} configurations. For the pure Li-rich SS1073R, the estimated enrichment matches well the value $y = 0.11$, as obtained from XRD data.

The particle size of the Li-rich phase should be rather small in the SG573 sample—about 20 nm from the M_{ii} and M_{ij} values (Fig. 3a)—and progressively larger with increasing T_A , as expected. The formation of stoichiometric and pure LiMn_2O_4 by the sol-gel method, completed at about 1073 K, is consistent with the small initial crystallite size of the early-enriched phase (first step of formation).

At $T_A < 1073$ K, the formation of spurious phases (manganese oxides) is consistent with the Li-enriched spinel phase (Table 1). These spurious phases can be related to the variations of RF vs T (Fig. 5b) in the EPR measurements. We already verified the shift of RF toward higher magnetic fields in samples containing even very small amounts of Mn_3O_4 (20). For SG573 the opposite trend at low temperature could be related to the large presence of Mn_5O_8 . The comparison between the χ_m curves of SG573 and SS1073R can give indication of the possible magnetic behavior of

² The magnetic susceptibility data by Schutte *et al.* (30) and our results are in good agreement.

$$\frac{1}{\chi} \cong 120 \frac{\text{mol}}{\text{cm}^3} \quad \text{at } T = 300 \text{ K, and } \vartheta = (-338 \pm 60) \text{ K} \quad (\text{Schutte } et al. (30))$$

$$\frac{1}{\chi} \cong 22,000 \frac{\text{g}}{\text{cm}^3} \cong 120 \frac{\text{mol}}{\text{cm}^3} \quad \text{at } T = 300 \text{ K, and } \vartheta = -320 \text{ K} \quad (\text{our data (13, 20)})$$

For LiMn_2O_4 , in the spin only ($g = 2$) approximation,

$$\chi_{\text{mol}} = \frac{N_A}{2} \frac{\mu_B^2 g^2}{3k_B(T - \vartheta)} [S_1(S_1 + 1) + S_2(S_2 + 1)],$$

where subscripts 1 and 2 refer to Mn^{4+} and Mn^{3+} ions, respectively, so that m^2 of a formula unit results in

$$\mu_B^2 g^2 [S_1(S_1 + 1) + S_2(S_2 + 1)] \cong 40 \mu_B^2. \quad [a]$$

As for Mn^{4+} (d^3 , $S_1 = 3/2$),

$$\mu_B^2 g^2 S_1(S_1 + 1) = 15 \mu_B^2, \quad [b]$$

from [a] and [b] the spin value of the Mn^{3+} ions results in $S_2 \cong 2.05$; i.e. a high-spin configuration for Mn^{3+} can be deduced. The effective number of μ_B per unit formula is $\sqrt{40} = 6.32$ according to Schutte *et al.* (30), but this value does not mean that 6.3 unpaired electrons are present in a unit formula and that, consequently, some Mn^{3+} ions in the sample are in the low-spin configuration.

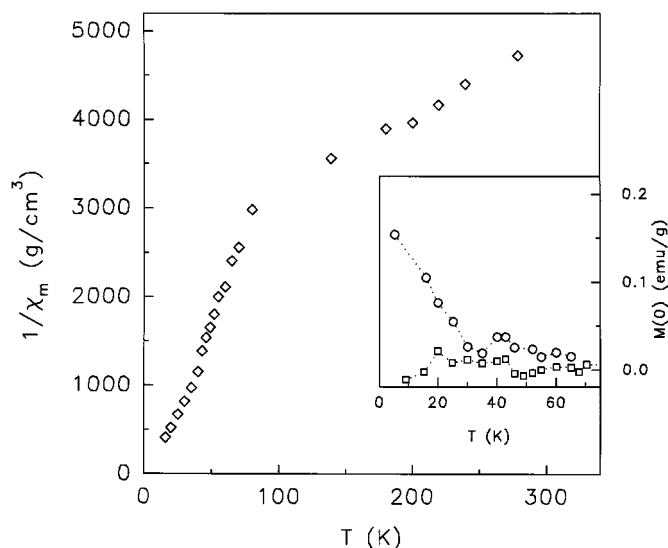


FIG. 7. Magnetic behavior of the Mn_5O_8 phase as deduced by subtraction between SG573 and SS1073R χ_m curves. The inset shows extrapolated mass magnetization curves vs temperature of SG573 (circles) and SS1073R (squares) samples.

the Mn_5O_8 phase. The difference between the χ_m data of SS1073R and SG573 samples, taking into account the phase percentage in SG573, suggests a ferrimagnetic-like behavior of Mn_5O_8 at $T < 30$ K (see Fig. 7), consistent with the RF shift of the EPR signal at low temperatures (see Fig. 5b).

5. CONCLUSIONS

XRD and conductivity results demonstrated that the sol-gel synthesis is suitable to obtain pure stoichiometric sample at 1073 K: this evidence is possibly related to the small initial crystallite size with respect to the solid state reaction. On the basis of this observation, a two-step mechanism can be proposed: small crystallite dimensions of Li-rich spinel phase and manganese oxides are formed at low temperature and successively react to form stoichiometric LiMn_2O_4 with increasing T_A . The evolution of the EPR, susceptibility, and conductivity data with changing T_A gives indication of effects of impurity phases and lithium enrichment of the spinel phase ($\text{Li}_{1+y}\text{Mn}_{2-y}\text{O}_4$).

ACKNOWLEDGMENTS

This work has been partially funded by Consorzio per i Sistemi a Grande Interfase (CSGI) and Progetto Finalizzato MSTA II of CNR.

REFERENCES

1. P. Barboux, J. M. Tarascon, and F. K. Shokoohi, *J. Solid State Chem.* **94**, 185 (1991).
2. J. M. Tarascon, W. R. McKinnon, F. Coowar, T. N. Bowmer, G. Amatucci, and D. Guyomard, *J. Electrochem. Soc.* **141**, 1421 (1994).
3. J. C. Hunter, *J. Solid State Chem.* **39**, 142 (1981).
4. M. M. Thackeray, P. J. Johnson, L. A. de Picciotto, P. G. Bruce, and J. B. Goodenough, *Mater. Res. Bull.* **19**, 179 (1984).
5. G. Pistoia, G. Wang, and C. Wang, *Solid State Ionics* **58**, 285 (1992).
6. G. A. Martin, A. Bates, V. Ducarme, and C. Mirodatos, *Appl. Catal.* **47**, 289 (1989).
7. C. Masquelier, M. Tabuchi, K. Ado, R. Kanno, Y. Kobayashi, Y. Macki, O. Nakamura, and J. B. Goodenough, *J. Solid State Chem.* **123**, 255 (1996).
8. A. Yamada, *J. Solid State Chem.* **122**, 160 (1996).
9. K. R. Morgan, S. Collier, G. Burns, and K. Ooi, *J. Chem. Soc. Chem. Commun.*, 1719 (1994).
10. P. Mustarelli, V. Massarotti, M. Bini, and D. Capsoni, *Phys. Rev. B* **55**, 12018 (1997).
11. V. Massarotti, M. Bini, and D. Capsoni, *Z. Naturforsch.* **51a**, 267 (1996).
12. V. Massarotti, D. Capsoni, M. Bini, C. B. Azzoni, and A. Paleari, *J. Solid State Chem.* **128**, 80 (1997).
13. C. B. Azzoni, M. C. Mozzati, A. Paleari, V. Massarotti, M. Bini, and D. Capsoni, *Z. Naturforsch.* **53a**, 771 (1998).
14. J. M. Tarascon and D. Guyomard, *Electrochim. Acta* **38**, 1221 (1994).
15. J. Sugiyama, T. Tamura, and H. Yamauchi, *J. Phys. Condens. Matter* **7**, 9755 (1995).
16. L. Chen and J. Schoonman, *Solid State Ionics* **67**, 17 (1994).
17. G. Pistoia, A. Antonini, R. Rosati, and D. Zane, *Electrochim. Acta* **41**, 2683 (1996).
18. S. Bach, J. Farcy, and J. P. Pereiramos, *Solid State Ionics* **110**, 193 (1998).
19. J. S. Lee, Y. K. Sun, and K. S. Nahm, *Solid State Ionics* **109**, 285 (1998).
20. C. B. Azzoni, M. C. Mozzati, A. Paleari, V. Massarotti, D. Capsoni, and M. Bini, *Z. Naturforsch.* **53a**, 693 (1998).
21. V. Massarotti, D. Capsoni, M. Bini, G. Chiodelli, C. B. Azzoni, M. C. Mozzati, and A. Paleari, *J. Solid State Chem.* **131**, 94 (1997).
22. D. B. Wiles and R. A. Young, *J. Appl. Crystallogr.* **14**, 149 (1981).
23. D. G. Wickham and W. J. Croft, *J. Phys. Chem. Solids* **7**, 351 (1958).
24. L. Lutterotti and P. Scardi, *J. Appl. Crystallogr.* **23**, 246 (1990).
25. V. Massarotti, M. Bini, D. Capsoni, P. Scardi, and M. Leoni, *Mater. Sci. Forum* **278-281**, 820 (1998).
26. C. B. Azzoni, M. C. Mozzati, A. Paleari, M. Bini, D. Capsoni, G. Chiodelli, and V. Massarotti, submitted.
27. H. Yamaguchi, A. Yamada, and H. Uwe, *Phys. Rev. B* **58**, 8 (1998).
28. A. Abragam and B. Bleaney, in "Electron Paramagnetic Resonance of Transition Ions," pp. 527-529. Clarendon, Oxford, 1970.
29. H. R. Oswald and M. J. Wampetich, *Helv. Chim. Acta* **50**, 2023 (1967).